Multicellular Sprouting In Vitro

Andras Szabo,* Elod Mehes,* Edina Kosa,* and Andras Czirok*†
*Department of Biological Physics, Eotvos University, Budapest, Hungary; and †Department of Anatomy & Cell Biology, University of Kansas Medical Center, Kansas City, Kansas

ABSTRACT Cell motility and its guidance through cell-cell contacts is instrumental in vasculogenesis and in other developmental or pathological processes as well. During vasculogenesis, multicellular sprouts invade rapidly into avascular areas, eventually creating a polygonal pattern. Sprout elongation, in turn, depends on a continuous supply of endothelial cells, streaming along the sprout toward its tip. As long-term videomicroscopy of in vitro cell cultures reveal, cell lines such as C6 gliomas or 3T3 fibroblasts form multicellular linear arrangements in vitro, similar to the multicellular vasculogenic sprouts. We show evidence that close contact with elongated cells enhances and guides cell motility. To model the patterning process we augmented the widely used cellular Potts model with an inherently nonequilibrium interaction whereby surfaces of elongated cells become more preferred adhesion substrates than surfaces of well-spread, isotropic cells.

INTRODUCTION

The collective motility of interacting cells is a poorly understood, but fundamental process during development. Arguably, cell sorting is the best understood process that involves the simultaneous displacement of multiple cell types (1). The differential adhesion hypothesis and its quantitative models—usually based on the Potts model of statistical physics (2,3)—successfully predict the outcome as well as the time-course of cell sorting experiments (4). Suitable extensions of these models can describe cell intercalation during gastrulation (5), chemotaxis-driven cell movements during vascular assembly (6–8), or tumor growth (9).

The formation of linear cell arrangements is a key step during vasculogenesis (10,11)—thus, the process is the focus of sustained interest. Two main mechanisms were proposed so far to explain vascular patterning.

1. The mechanochemical hypothesis assumes that cells exert mechanical stress on the underlying substrate, and the resulting stress guides cellular motility (12–14).
2. A more recent body of research focused on pattern emergence based on autocrine chemotactic signaling (6–8, 15,16).

Multicellular linear segments are also formed by a variety of cell types when grown under normal tissue culture conditions on a solid substrate (17). These simple systems can illuminate aspects of the sprouting mechanisms that are not covered by the mechanochemical or chemoattractant models. The rigid substrate excludes the mechanochemical mechanism. A specific chemotactic response is empirically unproven and unlikely to be shared by a great variety of cell types. Finally, convection currents in the culture medium—generated by temperature inhomogeneities within the incubator and the vibrations of microscope stage motion—are expected to hamper the maintenance of concentration gradients, or impose a strong directional bias upon the chemotaxis-related cell movements (17).

Motivated by the above observations and arguments, we recently proposed that multicellular sprouting behavior can involve a direct cell-cell interaction, which preferentially guides cells toward adjacent elongated cells (17). To show that such interaction can indeed generate linear segments and an interconnected network, we studied a model where cells are represented as point particles, and cell shape is only deduced from the configuration of surrounding cells.

Here we report detailed empirical data on the patterning process of multicellular segments in cultures of C6 glioma and 3T3 fibroblastlike cells. We show evidence that close contact with elongated cells indeed enhances and guides cell motility. To overcome the obvious shortcoming of the particle model, we also introduce a model which explicitly resolves cell shape based on the approach of Graner and Glazier (18). To adequately formulate the proposed preferential attraction to elongated cells, we augmented the transition probabilities of the cellular Potts model (CPM) with a new, inherently asymmetric term. The balance between multicellular sprouting and surface tension-driven coarsening is analyzed by systematic numerical simulations.

MATERIALS AND METHODS

Cell culture

C6 and 3T3 cells were cultured in DMEM (Sigma-Aldrich, St. Louis, MO) with 10% fetal calf serum (Gibco, Csertex, Budapest, Hungary) at 37°C in a 5% CO_2 atmosphere. Cells in multiple fields were observed for 35 h with automated phase-contrast time-lapse microscopy (19). Images were obtained in every 10 min at a resolution of 1.3 or 0.3 megapixels.

Segmentation

To detect cell bodies in phase contrast images, we implemented the two stage segmentation scheme of Wu et al. (20). Briefly, an approximate area en-

Submitted January 17, 2008, and accepted for publication May 21, 2008.

Address reprint requests to Andras Czirok, Tel.: 913-945-6683; E-mail: aczirok@kumc.edu.

Editor: Alexander Mogilner.

0006-3495/08/09/2702/09 $2.00

doi: 10.1529/biophysj.108.129668

closing the cells is selected first. The classification is based on the substantially higher brightness variation within and around the cells. In the second step, cell bodies are located as areas darker than the bright halo surrounding phase objects. Although this automatic procedure is not satisfactory for the identification of individual cells, it is sufficient for the detection of the morphology of cell-configurations (Fig. S1in Supplementary Material).

Cell density

Local cell density is determined as the volume fraction occupied by segmented cell clusters within a 50-μm-wide region, i.e., the ratio of the area occupied by the clusters and the selected region. As the segmentation algorithm does not localize cell boundaries well, to obtain a measure of confluence the volume fraction values are normalized by the maximal volume fraction value observed for the particular cell type.

Anisotropy measure

A measure of local anisotropy, $A(x)$, was calculated using the segmented and subsequently smoothened (low pass-filtered) image as described by Czirok et al. (21). Briefly, a diffusion process of a concentration field c is started with a steady point source at x. At each pixel r the diffusion coefficient $D(r)$ is determined by the brightness $h(r)$ of the input image and $c(r)$ as

$$D(r) = h(r)\Theta(c(r) - c_{\min}), \quad (1)$$

where Θ is the Heaviside step function. The $c_{\min}$ concentration threshold yields a well-defined propagating front which encloses a gradually increasing area around the point source. The growing area is characterized by its principal moments of inertia, $\mu \geq \nu$. If the area is circular (isotropic), these principal moments are of a similar magnitude. In contrast, highly elongated anisotropic structures result in dissimilar principal moments. The area is grown until its width, $\nu^{3/8}\mu^{-1/8}$, reaches a predefined value, the typical width of a single cell. The local anisotropy of the location at the point-source is then characterized as $A(x) = \sqrt{\mu/\nu} - 1$. Repeating the procedure for various positions x results in an anisotropy map, as shown in Fig. S1 *e*.

The $A(x)$ anisotropy maps are also calculated for synthetic patterns to prove that they indeed detect linear multicellular structures instead of individual elongated cells. The randomized patterns consisted of segmented cell clusters as objects placed randomly without overlap (see Fig. S1 *d*). For intermediate volume fractions, the average local anisotropy of the synthetic patterns was significantly lower than the corresponding mean anisotropy determined from images of actual cell configurations (Fig. S1, *g* and *h*). However, the synthetic patterns still exhibited a substantial anisotropy, reflecting frequent elongated cell shapes within the culture (Fig. S1 *f*).

Cell positions and displacements

The positions $x_i(t)$ of various cells i were determined by manually tracking the centroid in the recorded image sequence, i.e., in every 10 min in real time (t). The velocity, $v_i(t)$ was calculated as the net displacement of the centroid during a 1 h-long time interval: $v_i(t) = |x_i(t + \Delta t) - x_i(t)|/\Delta t$, where $\Delta t = 1$ h.

Structure factor

The structure factor was calculated from the spatial power spectrum $P(q)$ as

$$S(q) = P(q)/P_1(q), \quad (2)$$

where $P(q)$ is the radially averaged and Hanning-windowed power spectrum of the spatial pattern $\chi(x, y)$ as

$$P(q)\delta q = \left\langle \mathcal{F}_{2D}\left[\chi(x,y)\sin\left(\frac{\pi x}{L}\right)\sin\left(\frac{\pi y}{L}\right)\right]\right\rangle_{q<|\underline{q}|<q+\delta q}, \quad (3)$$

where the two-dimensional Fourier transformation is denoted by $\mathcal{F}_{2D}$ and $\langle \ldots \rangle_{q<|\underline{q}|<q+\delta q}$ represents the radial average. The form factor $P_1(q)$ was obtained in an analogous manner from randomized configurations.

EMPIRICAL RESULTS

As we reported earlier (17), various cell types, such as astroglia-derived C6 cells or 3T3 fibroblasts exhibit sprouting behavior—linear arrangements of multiple cells—when grown under standard culture conditions on a solid substrate (Fig. S1, *a* and *b*). The multicellular morphology can be statistically characterized by a sequence of image processing steps (21). First, the cell-occupied area is identified by a segmentation procedure (Fig. S1 *c*). A measure of local anisotropy, $A(x)$, is then calculated utilizing a diffusion process with a point source at x. The resulting anisotropy maps readily reveal the highly elongated, multicellular structures (Fig. S1 *e*). Cell density strongly influences the possible cell arrangements. As Fig. S1, *g* and *h*, reveals, at high densities cells fill the substrate and the anisotropy of their arrangement is low. At very low cell densities, no multicellular structures are present. Between these extremes, at an intermediate density (20% confluence), maximal anisotropy values indicate that cells often assemble into linear structures.

Time-lapse microscopic records revealed that the intensity of cell motion strongly correlates with the presence of adjacent, elongated, highly anisotropic structures (Fig. 1). As cell trajectories demonstrate (Fig. 1 *a* and Movie S1 in Supplementary Material), cells intensively move toward and within extending sprouts. After the sprouts became wider, cell motility diminishes again. Movie S2 depicts a typical example when cell motility is initiated and guided by a contact of an elongated cell process.

To establish the correlation between cell motility and local anisotropy, individual cell velocity $v_i(t)$ values were paired with the calculated values of local anisotropy, $A_i(x_i(t))$, for various time points t and cells i. As Fig. 1 *b* demonstrates, cells tend to be up to three times faster in sprouts than in isotropic cell clusters.

An investigation of branch widening rates reveals that highly anisotropic structures are attractive migration targets. This preference is reflected in Fig. 1 *c* as the width of highly elongated and thus anisotropic sprouts increases at a faster rate. As we do not observe any obvious spatial pattern in cell division rate (data not shown), increased sprout widening is thus resulted by an increased immigration of cells. In summary, the data in Fig. 1 demonstrate that cells preferentially abandon contacts with well-spread cells and move toward adjacent elongated, anisotropic cells.

Asymmetric cellular Potts model

To formulate and test the hypothesis that multicellular patterning is resulted by elongated cell-guided motility, we modified the two-dimensional cellular Potts model (18). The advantage of the Potts formulation is that cell shape is ex-

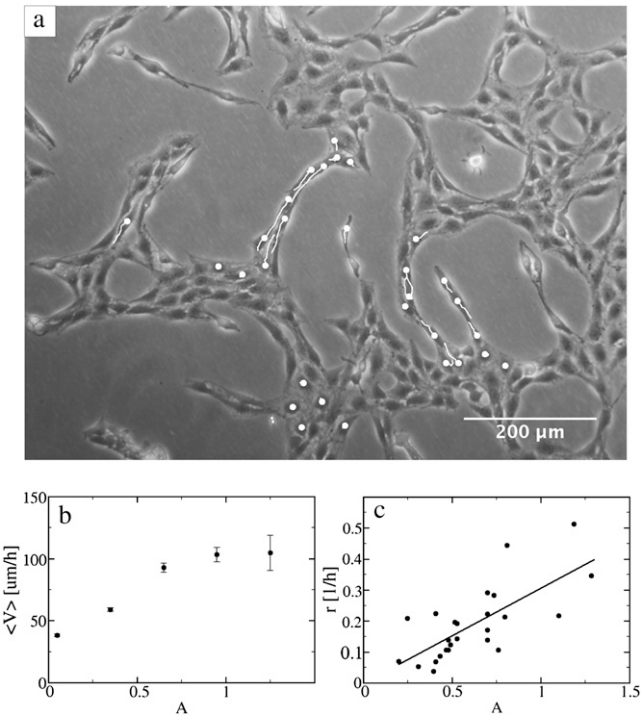

FIGURE 1 The dynamics of sprout formation in C6 cell cultures is visualized by time-lapse microscopy. (*a*) Cell trajectories demonstrate intense motility within elongated structures. Current cell positions are marked with open circles, trajectories are represented by open lines. Representative frame is taken from Movie S1. (*b*) Data obtained from 3000 manually traced positions of >50 C6 cells reveal that mean cell velocity is three times greater in highly anisotropic sprouts. Error bars represent the standard error of the mean. (*c*) The manually determined rate of branch widening is also positively correlated to the average anisotropy of the branch. The increased widening reflects increased migration into the branches.

plicitly resolved: distinct cells are represented as domains of the Potts model, i.e., a set of lattice sites x where each spin σ is of the same value. For cell i ($1 \le i \le N$), it is convenient to choose the common spin value as the cell index, $\sigma(x) = i$. The area devoid of cells is represented by spins with a special value $\sigma = 0$. The measure of anisotropy for cell i is θ_i, obtained from the inertia tensor of the Potts domain representing the cell as

$$\theta_i = (\mu_i/\nu_i)^{1/2} - 1, \tag{4}$$

where $\mu_i \ge \nu_i$ are the two eigenvalues of the inertia tensor. As the behavior of cells is, in many respects, dissimilar to that of the medium, we introduce the function χ to distinguish between the two: $\chi(x) = 0$ where $\sigma(x) = 0$, and $\chi(x) = 1$ elsewhere.

Cell movement is resulted from a series of elementary steps. Each step is an attempt to copy the spin value from a random lattice site to an adjacent site. The possible steps satisfy constraints ensuring that the domains which represent cells remain simply connected. Thus, cells cannot break into parts and no holes can form inside the cells. The model dynamics is specified through probabilities assigned to the various potential steps. The probability assignment rule ensures 1), the maintenance of a target cell size; 2), the adhesion of cells; and 3), cell motion tendencies, such as directed motility.

Motivated by the Metropolis Monte Carlo dynamics of the analogous Potts model, $p(a \to b)$, the probability of copying the spin value $\sigma(a)$ at lattice site a to an adjacent lattice site b, is given by a combination of two factors,

$$\ln p(a \to b) = \min(0, -\Delta u(a \to b) + w(a \to b)), \tag{5}$$

where Δu is the change in energy of the whole system according to the CPM (18) and w is a correction containing an asymmetric interaction bias.

The CPM energy of a given configuration, u, is minimal in configurations where cell adhesion and cell area preferences are met:

$$u = \alpha \sum_{\substack{\langle i,j\rangle \\ \sigma(i)\neq\sigma(j)}} J(\sigma(i),\sigma(j)) + \sum_{k=1}^{N} \lambda_k (\delta A_k)^2. \tag{6}$$

The first term in Eq. 6 is a weighted sum of the length of cell-cell and cell-medium boundaries. Formally, $J(\sigma(i),\sigma(j)) = \tilde{J}_{\chi(i),\chi(j)}$ is a ferromagnetic interaction between adjacent spins i and j belonging to different Potts domains. The $\tilde{J}$ interaction matrix is symmetric with one adjustable parameter β as

$$\tilde{J} = \begin{pmatrix} 0 & 1 \\ 1 & \beta \end{pmatrix}. \tag{7}$$

Parameter $\alpha > 0$ determines the relative weight of the effective surface tension in Eq. 6, while parameter β specifies the preference of cell-cell connections over cell-medium boundaries. For $\beta > 1$ or $\beta < 1$, cell-medium boundaries are preferred or penalized, respectively.

The second term in Eq. 6 is responsible for maintaining a target cell size. The deviation of the i^{th} cell's area from a specified target size is denoted by δA_i. The λ parameters are analogous to elastic moduli, and may depend on the measure of cell elongation to reflect assumptions that elongated cells tend to be stiffer.

The motion bias $w(a \to b)$ represents a tendency to contact elongated cells,

$$w(a \to b) = \gamma[\chi(a) - \chi(b)] \sum_{\substack{c \\ \sigma(c)\notin\{0,\sigma(a),\sigma(b)\}}} \theta_{\sigma(c)}, \tag{8}$$

where parameter γ sets the strength of the bias. The $\chi(a) - \chi(b)$ expression ensures that only cells (and not the medium) exhibit the preference. Furthermore, the expression also assumes that the amount of attraction depends only on the contact target: if site b is occupied by a cell ($\chi(b) = 1$), then no other cell ($\chi(a) = 1$) has any advantage to occupy that adhesion site. The summation in Eq. 8 goes over only those neighbor sites of b that belong to cells other than $\sigma(a)$ and $\sigma(b)$.

The $w(a \rightarrow b)$ term can also be considered as an asymmetric extension of the J adhesive interaction. This is more obvious if $w(a \rightarrow b)$ is written in the form of

$$w(a \rightarrow b) = -\gamma \sum_{c} [J_1^{a \rightarrow b}(\sigma(a), \sigma(c)) - J_1^{a \rightarrow b}(\sigma(b), \sigma(c))], \tag{9}$$

where

$$J_1^{a \rightarrow b}(i,j) = \begin{cases} 0 & \text{if } i = j,\ i = 0,\ j = 0,\ j = a \text{ or } j = b; \\ \theta_j & \text{otherwise.} \end{cases} \tag{10}$$

In general, $\theta_i \neq \theta_j$, thus J_1 is an asymmetric matrix. The asymmetry is instrumental in transforming the model into a stochastic system where configuration and transition probabilities do not satisfy detailed balance. As the example in Fig. 2 demonstrates, configuration (d) can be reached by at least two different sequences of steps from configuration (a). Due to symmetry, the p transition probabilities between states (a) and (b) are the same as those between (a) and (c). However, if cell A is more attractive than cell B, then the $(b) \rightarrow (d)$ transition is more frequent than the $(c) \rightarrow (d)$ transition. Furthermore, the $(d) \rightarrow (b)$ transition is less frequent than the $(d) \rightarrow (c)$ transition:

$$\frac{p((b) \rightarrow (d))}{p((c) \rightarrow (d))} > 1 > \frac{p((d) \rightarrow (b))}{p((d) \rightarrow (c))}. \tag{11}$$

If the equilibrium probability of states (b), (c), and (d) are P, P, and Q, respectively, then the detailed balance condition requires $Pp((b) \rightarrow (d)) = Qp((d) \rightarrow (b))$ and $Pp((c) \rightarrow (d)) = Qp((d) \rightarrow (c))$. However, the resulting

$$\frac{p((b) \rightarrow (d))}{p((c) \rightarrow (d))} = \frac{p((d) \rightarrow (b))}{p((d) \rightarrow (c))} \tag{12}$$

condition contradicts Eq. 11. Therefore, in the asymmetric model, the transition probabilities cannot satisfy the detailed balance condition, and thus the dynamics cannot be interpreted as relaxation of an energy functional to thermal equilibrium.

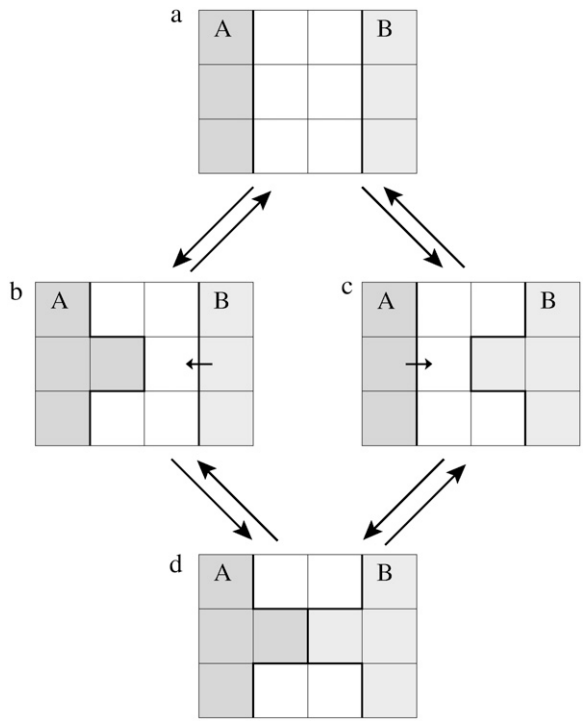

FIGURE 2 Demonstration of the asymmetric interaction. By symmetry arguments the first step has the same probability in both paths: $p((a) \rightarrow (b)) = p((a) \rightarrow (c))$ and $p((b) \rightarrow (a)) = p((c) \rightarrow (a))$. However, if cell A is more attractive than cell B, then the $(b) \rightarrow (d)$ transition is more frequent than the $(c) \rightarrow (d)$ transition (indicated by *arrows* in b and c, respectively). Furthermore, the $(d) \rightarrow (b)$ transition is less frequent than the $(d) \rightarrow (c)$ transition. As a result, the steady-state probabilities of the four configurations will not satisfy detailed balance.

SIMULATION RESULTS

The model was studied by simulations in a square area of size L^2 with closed boundary conditions. The initial configuration consisted of N randomly positioned, but simply-connected domains representing cells and an arbitrary domain representing the cell-free areas on the substrate. The preferred cell size is 50 lattice sites, thus the distance of two lattice points is $\sim 1\ \mu$m. A Monte Carlo (MC) time-step in the model is defined as L^2 spin conversion attempts. This time unit corresponds to ~ 2 min in real time—revealed by the comparison of simulated and empirical (see, e.g., (22)) mean-square displacement versus time curves of noninteracting cells.

For certain parameter values, the model indeed exhibits branch sprouting behavior, reminiscent of those observed in experiments (Fig. 3). After the initial bud appears, the leading (elongated) cells attract other cells from the pool at the base of the sprout. Cells constituting the sprout continue to migrate until they connect to another cluster of cells. At that point, the branch is established and becomes stable. Due to the effective surface tension present in the system (23), branches can also break up, resulting in a coarsening effect.

If sprouting takes place in the system, then after an initial transient regime the balance of surface tension-driven coarsening and the growth of new branches results in a quasistationary state (Fig. 4 and Movie S3). As the ensemble-averaged structure factors $S(q)$ indicate (Fig. 4 d), after the first 1000 MC time-steps the statistical properties of the networklike pattern does not change substantially. The characteristic pattern size $\ell \approx 80$ is determined by the dynamics, and does not depend on the system size for $L \gg \ell$ (Fig. 4 e).

The effects of the symmetric and asymmetric adhesion terms in Eq. 6 were studied systematically with simulations. Parameter γ, characterizing the preference of elongated cells,

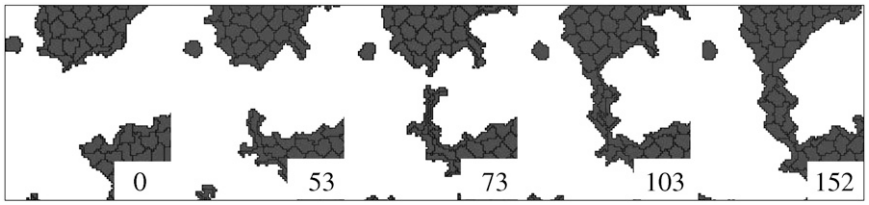

FIGURE 3 Formation of new branches in the stationary state of the model. Fluctuations initiate sprouts, and the resulting elongated structure attracts further cells. If the expanding branch connects to another cluster it becomes stable, otherwise it degenerates. In a typical example, time shown is indicated in MC time-steps.

is responsible for sprouting activity in the model (Fig. 5 *a*). As cell-cell contacts increase the CPM energy u by $\alpha\beta$, an effective attraction requires $\gamma > \alpha\beta$. For a fixed value of γ, the two independent parameters α and β control the effective surface tension, and thus the characteristic pattern size (Fig. 5 *b*). Cell shape is determined by the relative balance of surface tension and anisotropic bias: if anisotropic bias dominates, individual cells become extremely elongated.

For a fixed value of model parameters, cell density determines the interconnectedness of the structure, and it also influences the characteristic pattern size (Fig. 6 *a*). Cell density is measured as a volume fraction, i.e., the ratio of the area covered by cells and the overall simulation area. At densities higher than 55%, the linear structures gradually disappear. At densities under 20%, there are not enough cells to form interconnecting clusters. As in the case of the analogous particle model (17), within an intermediate range of densities, the characteristic pattern size ℓ depends only weakly on the density (Fig. 6 *b*).

The local anisotropy of the configuration was calculated as the function of the local volume fraction for a range of cell densities (Fig. 6 *c*). At low densities, the anisotropy tends to be higher, and it exhibits a maximum at a density ≈40%. The peaked curve is thus qualitatively similar to the empirical data (Fig. S1, *g* and *h*). The lower values of anisotropy reflect the fact that branches in the model are usually more than single-cell-wide.

The energy expression, Eq. 6, contains elasticlike terms involving δA_i, the deviation of the i^{th} cell's area from its target value. Thus, δA can be interpreted as a measure of hydrostatic pressure. In the recently proposed model of Merks et al. (6,8), branching occurs due to an instability which involves the internal, hydrostaticlike pressure within the aggregates and a radially weakening effective surface tension. To compare this patterning mechanism to that of Merks et al., we characterized cell compressions in both models. The distributions of δA are shown in Fig. 7 *a*. As expected, cells in the Merks model are under compression. In contrast, cell areas in our model fluctuate around the target size, with slightly more expanded cells then compressed cells. Fig. 7 *b* shows the distribution of compressed (*solid*) and expanded (*light shaded*) cells in a typical configuration generated by our model. The random mixture of compressed and expanded cells also indicate that hydrostatic pressure

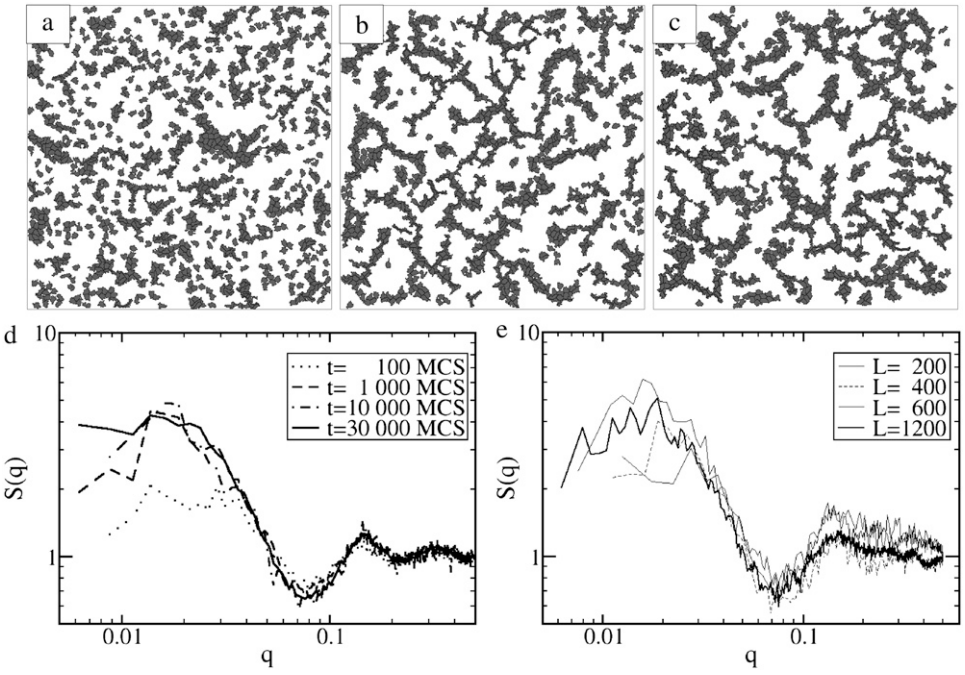

FIGURE 4 The model reaches a stationary state where surface tension-driven coarsening is balanced by the formation of new sprouts. Configurations in the model are shown after 100 (*a*), 1000 (*b*), and 30,000 (*c*) MC time-steps. As the structure factors averaged over 10 independent runs reveal, the emerged pattern does not change its statistical characteristics after 1000 steps (*d*). However, the resulting pattern is not frozen: branches still form and break up, as visualized in Fig. 3. The characteristic pattern size $\ell \approx 80$ is independent of the system size L in the $L \gg \ell$ limit as the structure factors of configurations obtained from systems with increasing sizes indicate (*e*).

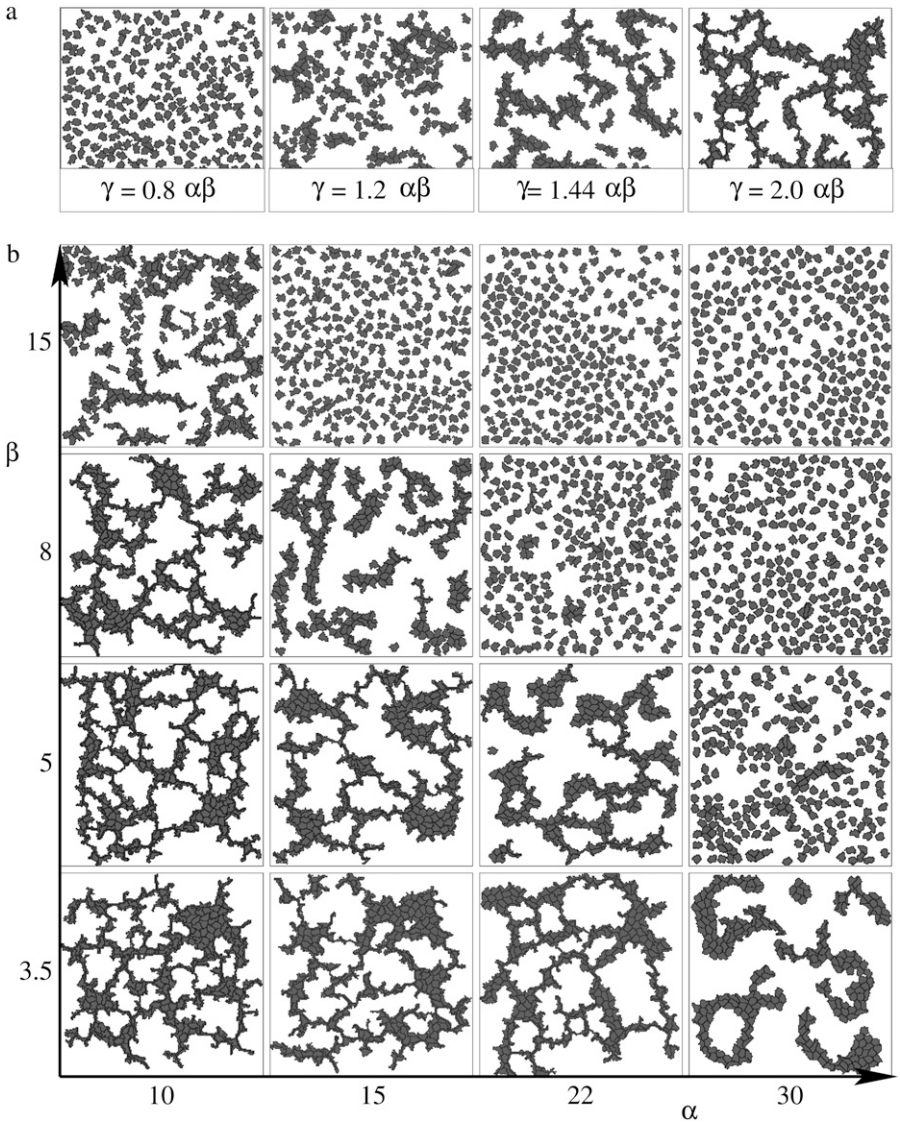

FIGURE 5 Morphology diagram of the stationary state as a function of γ, the strength of attraction to elongated cells, and parameters α and β specifying an effective surface tension in the model. (*a*) For $\gamma > \alpha\beta$, an interconnected pattern arises. Typical configurations are shown for $\alpha = 15$ and $\beta = 8$. (*b*) For a fixed $\gamma = 180$, increasing α results in coarser structures, while increasing β yields individual cells above the $\gamma = \alpha\beta$ threshold. The parameters are $L = 200$ and $N = 250$.

cannot play a substantial role within our model. Thus, the two models generate branching structures in clearly different regimes of the CPM.

DISCUSSION

Attraction to elongated cells

Here we provided statistical evidence that various cell types such as C6 gliomas or 3T3 fibroblasts form multicellular linear arrays in a certain range of cell densities. This patterning cannot be explained by the usual models of random motility and isotropic cell-cell adhesion which predicts gradually growing droplets (24). By the analysis of time-lapse recordings we showed here, for the first time of which we are aware, the remarkable change in cell motility when cells become incorporated into multicellular sprouts, and that these sprouts are attractive migration targets: due to cell migration, the population of sprouts increases substantially faster than the population of isotropic cell groups. As highly elongated cells initiate and guide the motility of adjacent cells, we argue that the generic ability to form cellular networks can be attributed to this preferential attraction to elongated cells.

The cell biological basis for such a preference is not yet known. We speculate that cells in elongated structures are under mechanical tension, and strained cells can have a stiffer cytoskeleton (25). Cells are able to respond to variations in extracellular matrix stiffness (26), and an analogous mechanotaxis utilizing cell-cell contacts is also feasible. For example, VE-cadherin, a major cell-cell adhesion receptor of vascular endothelial cells, was recently shown to be incorporated in cell-surface mechanosensing complexes (27). Mechanosensing, the detection of extracellular mechanical properties, usually involves myosin II-based traction force generation (28). Treating both 3T3 or C6 cells with bleb-

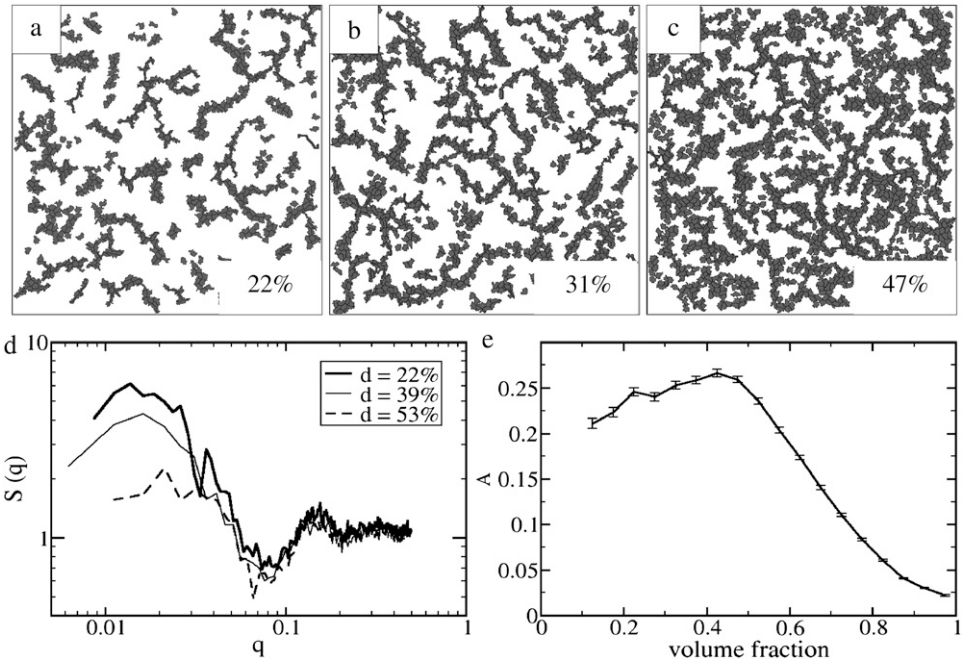

FIGURE 6 The stationary pattern depends on the volume fraction. Typical model configurations are shown for volume fractions of 22% (*a*), 31% (*b*), and 47% (*c*). The normalized structure factors (*d*) reveal a peak at $\ell \approx 80$ for densities between 30% and 50%. The local anisotropy of the configuration as the function of the local volume fraction (*e*) reveals a maximum at a density ≈40%. The peaked curve is thus qualitatively similar to the empirical data (Fig. S1, *g* and *h*). The parameters are $\alpha = 15, \beta = 8, \gamma = 1.5\alpha\beta$, and $L = 400$.

bistatin, a potent myosin II inhibitor, indeed disrupts the multicellular sprouts despite the highly elongated morphology of the individual blebbistatin-treated cells (data not shown).

Numerical modeling

In Szabo et al. (17), some aspects of the preferential attraction interaction were studied with a simple model representing cells as interacting point particles. Here we formulate our hypothesis using the cellular Potts model (CPM, (2)). As each modeling attempt of a multicellular system introduces hidden, implicit assumptions on cell motility and cell-cell interactions, we argue that it is intrinsically valuable to cast the biologically relevant hypothesis into very different modeling frameworks, and show that the emergent multicellular behavior is independent of the choice of framework. Furthermore, the particle model does not resolve cell shape (in fact, it models attraction to anisotropic micro-environments, where anisotropy is inferred from the configurations of not necessarily adjacent cells within a fixed range). Because cell surfaces interact with the local molecular environment (surfaces of other cells or extracellular matrix structures), in Szabo et al. (17) a further assumption had to be made, which ensures that the anisotropy of cell configurations is somehow manifested at the level of individual cells. The CPM formulation, in contrast, allows the explicit representation of our hypothesis and is truly local in the sense that only adjacent cells interact. The CPM formulation also yields novel insights or predictions less readily available from other models. As the CPM is especially suitable to study cell-cell adhesion (2), the demonstration of the competing effects of surface tension and the attraction to elongated cells (Fig. 5) would be much harder using the particle model. Finally, due to the wide use of the Potts formalism, comparison between models built upon the same framework (see, e.g., Fig. 7) are more feasible. Unfortunately, in the CPM formulation the factors determining cell motility are hidden in the stochastic simulation rules and are thus less transparent.

To account for the preferential attraction of elongated cells, we augmented the CPM with transition probabilities that

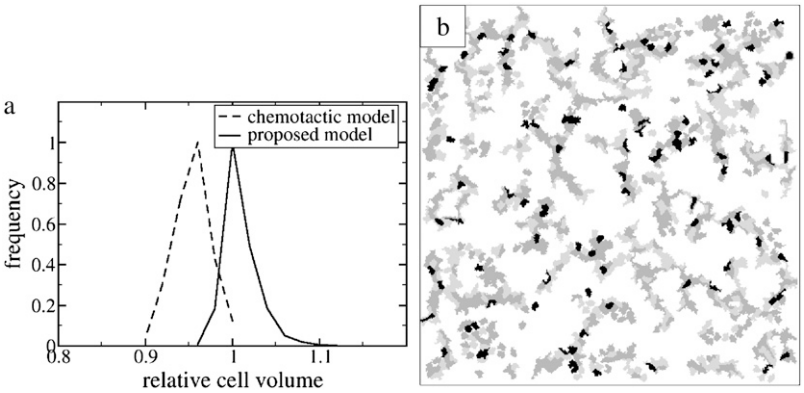

FIGURE 7 In the proposed model the patterning mechanism differs from the chemotactic model of Merks et al. (6). (*a*) The size distribution of the simulated cells reveals that in our model the cells are not compressed, but are rather elongated. (*b*) The location of stretched (*light shading*) and compressed (*solid*) cells show no obvious regularity within a typical configuration. Cells with the target area are shown as medium shading.

depend on the actual state of interaction partners. The asymmetric attraction term in the transition probabilities results in an inherently nonequilibrium system. This cell shape-dependent attraction is fundamentally different from the anisotropic interaction suggested by Zajac et al. (5), where the dynamics (apart from the continuity constraints) can still be derived as a relaxation of an energy functional of the spin configurations. However, it is not clear why such a global target/cost function should always exist to describe the behavior of multicellular systems—nonequilibrium transition rules may be useful to model other systems as well.

Patterning through sprouting—as predicted by our hypothesis and found both in vivo and in vitro—is markedly different from the gradual coarsening of an initially uniform density field and its possible arrest, characteristic for colloid gels (see, e.g., (29)) or for several models proposed to describe vasculogenesis. In particular, a frozen pattern was reported to gradually emerge, with an increasing modulation amplitude in cell density, in the mechanochemical model (see Fig. 6, of (12), or Fig. 7 of (31)). Gradually increasing avascular area sizes were reported in the autocrine chemoattractant model (Fig. 1 of Serini et al. (16)). Except for a recent model with autocrine chemotaxis and contact inhibition (8), none of these models were reported to produce sprouts. Sprouts are also predicted by a patterning method which assumes a prepattern of extracellular matrix molecules to guide cell migration (32). However, all empirical evidence points to the lack of such a mechanism either during in vivo vasculogenesis (11) or in our simple cell cultures grown on a solid surface. In the latter case, serum proteins adhere strongly to the plastic surface and thus cannot be rearranged (prepatterned) without the close proximity of cells.

Mechanism of sprout formation

Our model predicts a quasistationary state in which networklike patterns are produced without any of the external fields of the previous models of vasculogenesis. As morphology measures such as the local anisotropy A reveal, the model-generated patterns are similar to the networks exhibited by several cells in vitro. The hypothesis assuming preferential attraction to elongated cells results in linear structures by two means: increased probability of multicellular sprout formation; and increased stability of links already connecting two clusters.

1. An expanding multicellular sprout clearly needs a supply of cells from the reservoir at the sprout base. As invading cells are elongated, they thus attract additional cells into the sprout. Cell-cell adhesion alone would keep those cells at the sprout base where they are well surrounded with neighbor cells.
2. It is well known that cell-cell adhesion can be well described as an effective surface tension (24). Surface tension drives the system to minimize open surfaces (i.e., cell surfaces unattached to adjacent cells), hence it works to destroy sprouts. When a branch connecting two clusters is about to break, it will consist of elongated (and strained) cells which bridge between the clusters and adhere to both. According to our hypothesis, such a cell is an attractive migration target and the resulting active inflow of cells into the strained area will offset the coarsening tendency of surface tension.

The typical pattern size is thus partially determined by the two competing effects: larger surface tension results in a coarser structure with large void areas and thick branches as Fig. 5 demonstrates. Furthermore, the typical branch length is also influenced by the kinetic parameters of cell motility, especially its persistence length. In this work, we considered a simple case where cells perform random motility without persistence, therefore sprout tip cells do not migrate deep into empty areas. A modification of the presented model where cells perform persistent random walks, however, predicts that increased persistence yields longer sprouts (data not shown).

Since the recent model of Merks et al. (8) also results in sprouts with biologically plausible assumptions, we devoted special care to show that the two models operate in distinct parameter regimes and utilize different mechanisms (Fig. 7). The most striking difference is that the chemotaxis-based model is pressure-driven, and cells are predicted to be compressed in the aggregates. Patterning occurs due to an instability which involves the internal, hydrostaticlike pressure within the aggregates and a radially weakening effective surface tension. Therefore, aggregate surfaces are unstable and sprouting is driven by an internal pressure gradient. In contrast, in our model cells are typically not compressed, which prevents the buildup of pressure gradients within the aggregates. We argue, that our approach fits better the in vitro cell cultures with low cell densities—where cells are well-spread or moderately stretched—based on the well-known reduction of cell area after severing cell attachments to the substrate, e.g., by trypsin treatment.

A major question in developmental biology is the formation of structures from individual, smaller scale units. This problem is present through the subcellular level to the organizational level of tissues and organs. In this article, we dealt with the emergence of a multicellular structure: the formation of linear segments and networks of cells in vitro. Our results suggest that besides chemotactic effects, a preferential adhesion toward elongated cells can also contribute to the multicellular sprouting during vasculogenesis (10,11).

SUPPLEMENTARY MATERIAL

To view all of the supplemental files associated with this article, visit www.biophysj.org.

We are grateful to Charles D. Little and Tamas Vicsek for valuable discussions, and to Roeland H. Merks for generously sharing his simulation

code with us. A.C. is grateful for the hospitality of James A Glazier's group during his visit at Indiana University.

This work was supported by the National Institutes of Health (grant No. R01 HL87136), the American Heart Association (grant No. SDG 0535245N), and the Hungarian National Office for Research and Technology.

REFERENCES

1. Foty, R. A., and M. S. Steinberg. 2005. The differential adhesion hypothesis: a direct evaluation. *Dev. Biol.* 278:255–263 http://dx.doi.org/10.1016/j.ydbio.2004.11.012.
2. Glazier, J. A., and F. Graner. 1993. Simulation of the differential adhesion driven rearrangement of biological cells. *Phys. Rev. E Stat. Phys. Plasmas Fluids Relat. Interdiscip. Top.* 47:2128–2154.
3. Izaguirre, J. A., R. Chaturvedi, C. Huang, T. Cickovski, J. Coffland, G. Thomas, G. Forgacs, M. Alber, G. Hentschel, S. A. Newman, and J. A. Glazier. 2004. CompuCell, a multi-model framework for simulation of morphogenesis. *Bioinformatics.* 20:1129–1137 http://dx.doi.org/10.1093/bioinformatics/bth050.
4. Alber, M., N. Chen, T. Glimm, and P. M. Lushnikov. 2006. Multiscale dynamics of biological cells with chemotactic interactions: from a discrete stochastic model to a continuous description. *Phys. Rev. E Stat. Nonlin. Soft Matter Phys.* 73:051901.
5. Zajac, M., G. L. Jones, and J. A. Glazier. 2003. Simulating convergent extension by way of anisotropic differential adhesion. *J. Theor. Biol.* 222:247–259.
6. Merks, R. M., S. V. Brodsky, M. S. Goligorksy, S. A. Newman, and J. A. Glazier. 2006. Cell elongation is key to in silico replication of in vitro vasculogenesis and subsequent remodeling. *Dev. Biol.* 289:44–54.
7. Bauer, A. L., T. L. Jackson, and Y. Jiang. 2007. A cell-based model exhibiting branching and anastomosis during tumor-induced angiogenesis. *Biophys. J.* 92:3105–3121.
8. Merks, R., E. Perryn, and J. Glazier. 2007. Contact-inhibited chemotactic motility: role in de novo and sprouting blood vessel growth. Http://arxiv.org/ftp/q-bio/papers/0505/0505033.pdf.
9. Drasdo, D., and S. Hohme. 2003. Individual-based approaches to birth and death in avascular tumors. *Math. Comput. Model.* 37:1163–1175.
10. Perryn, E. D., A. Czirok, and C. D. Little. 2007. Vascular sprout formation entails tissue deformations and VE-cadherin-dependent cell-autonomous motility. *Dev. Biol.* In press.
11. Rupp, P. A., A. Czirok, and C. D. Little. 2004. $\alpha v\beta 3$ integrin-dependent endothelial cell dynamics in vivo. *Development.* 131:2887–2897.
12. Manoussaki, D., S. R. Lubkin, R. B. Vernon, and J. D. Murray. 1996. A mechanical model for the formation of vascular networks in vitro. *Acta Biotheor.* 44:271–282.
13. Murray, J. D. 2003. Mathematical Biology, 2nd Ed. Springer Verlag, Berlin.
14. Murray, J. D., D. Manoussaki, S. R. Lubkin, and R. Vernon. 1998. A mechanical theory of in vitro vascular network formation. *In* Vascular Morphogenesis: in Vivo, in Vitro, in Mente. C. D. Little, V. Mironov, and E. H. Sage, editors. Birkhauser, Boston, MA.
15. Gamba, A., D. Ambrosi, A. Coniglio, A. de Candia, S. Di Talia, E. Giraudo, G. Serini, L. Preziosi, and F. Bussolino. 2003. Percolation, morphogenesis, and burgers dynamics in blood vessels formation. *Phys. Rev. Lett.* 90:118101.
16. Serini, G., D. Ambrosi, E. Giraudo, A. Gamba, L. Preziosi, and F. Bussolino. 2003. Modeling the early stages of vascular network assembly. *EMBO J.* 22:1771–1779.
17. Szabo, A., E. D. Perryn, and A. Czirok. 2007. Network formation of tissue cells via preferential attraction to elongated structures. *Phys. Rev. Lett.* 98:038102.
18. Graner, F., and J. A. Glazier. 1992. Simulation of biological cell sorting using a two-dimensional extended Potts model. *Phys. Rev. Lett.* 69:2013–2016.
19. Czirók, A., K. Schlett, E. Madarász, and T. Vicsek. 1998. Exponential distribution of locomotion activity in cell cultures. *Phys. Rev. Lett.* 81:3038–3041.
20. Wu, K., D. Gauthier, and M. D. Levine. 1995. Live cell image segmentation. *IEEE Trans. Biomed. Eng.* 42:1–11.
21. Czirok, A., E. A. Zamir, A. Szabo, and C. D. Little. 2007. Multicellular sprouting during vasculogenesis. *Curr. Top. Dev. Biol.* 81:269–289.
22. Stokes, C. L., D. A. Lauffenburger, and S. K. Williams. 1991. Migration of individual microvessel endothelial cells: stochastic model and parameter measurement. *J. Cell Sci.* 99:419–430.
23. Foty, R., G. Forgacs, C. Pfleger, and M. Steinberg. 1994. Liquid properties of embryonic tissues: measurement of interfacial tensions. *Phys. Rev. Lett.* 72:2298–2301.
24. Beysens, D. A., G. Forgacs, and J. A. Glazier. 2000. Cell sorting is analogous to phase ordering in fluids. *Proc. Natl. Acad. Sci. USA.* 97:9467–9471.
25. Xu, J., Y. Tseng, and D. Wirtz. 2000. Strain hardening of actin filament networks. Regulation by the dynamic cross-linking protein α-actinin. *J. Biol. Chem.* 275:35886–35892.
26. Gray, D., J. Tien, and C. Chen. 2003. Repositioning of cells by mechanotaxis on surfaces with micropatterned Young's modulus. *J. Biomed. Mater. Res. A.* 66:605–614.
27. Tzima, E., M. Irani-Tehrani, W. B. Kiosses, E. Dejana, D. A. Schultz, B. Engelhardt, G. Cao, H. DeLisser, and M. A. Schwartz. 2005. A mechanosensory complex that mediates the endothelial cell response to fluid shear stress. *Nature.* 437:426–431.
28. hui Guo, W., M. T. Frey, N. A. Burnham, and Y. li Wang. 2006. Substrate rigidity regulates the formation and maintenance of tissues. *Biophys. J.* 90:2213–2220.
29. Foffi, G., C. De Michele, F. Sciortino, and P. Tartaglia. 2005. Arrested phase separation in a short-ranged attractive colloidal system: a numerical study. *J. Chem. Phys.* 122:224903.
30. Reference deleted in proof.
31. Namy, P., J. Ohayon, and P. Tracqui. 2004. Critical conditions for pattern formation and in vitro tubulogenesis driven by cellular traction fields. *J. Theor. Biol.* 227:103–120.
32. Vernon, R., S. Lara, C. Drake, M. Iruela-Arispe, J. Angello, C. Little, T. Wight, and E. Sage. 1995. Organized type I collagen influences endothelial patterns during ''spontaneous angiogenesis in vitro'': planar cultures as models of vascular development. *In Vitro Cell. Dev. Biol. Anim.* 31:120–131.